Acta Crystallographica Section A
Foundations of Crystallography
ISSN 0108-7673

Received 30 June 2009
Accepted 30 September 2009

This article is dedicated to the memory of Dr David Sadler of Bristol University Physics Department, who lectured to my undergraduate class on the subject of the DSE in 1980.

A new approach to calculating powder diffraction patterns based on the Debye scattering equation

Noel William Thomas

Fachhochschule Koblenz, Fachbereich Ingenieurwesen, Fachrichtung Werkstofftechnik Glas und Keramik, Rheinstrasse 56, 56203 Höhr-Grenzhausen, Germany. Correspondence e-mail: thomas@fh-koblenz.de

A new method is defined for the calculation of X-ray and neutron powder diffraction patterns from the Debye scattering equation (DSE). Pairwise atomic interactions are split into two contributions, the first from lattice-pair vectors and the second from cell-pair vectors. Since the frequencies of lattice-pair vectors can be directly related to crystallite size, application of the DSE is thereby extended to crystallites of lengths up to ~200 nm. The input data correspond to unit-cell parameters, atomic coordinates and displacement factors. The calculated diffraction patterns are characterized by full backgrounds as well as complete reflection profiles. Four illustrative systems are considered: sodium chloride (NaCl), α-quartz, monoclinic lead zirconate titanate (PZT) and kaolinite. The effects of varying crystallite size on diffraction patterns are calculated for NaCl, quartz and kaolinite, and a method of modelling static structural disorder is defined for kaolinite. The idea of partial diffraction patterns is introduced and a treatment of atomic displacement parameters is included. Although the method uses pair distribution functions as an intermediate stage, it is anticipated that further progress in reducing computational times will be made by proceeding directly from crystal structure to diffraction pattern.

1. Introduction

Relatively little attention has been given to the Debye scattering equation (DSE) (Debye, 1915) as a means of calculating the diffraction patterns of polycrystalline samples from first principles. His equation may be stated as follows.

$$I(Q) = \sum_m \sum_n f_m f_n [\sin(Qr_{mn})/Qr_{mn}]. \quad (1)$$

Here $I(Q)$ represents the intensity of scattering at wavevector magnitude Q. The latter is linked to the scattering angle, 2θ, and the wavelength of the radiation, λ, by the relationship $Q = 4\pi \sin\theta/\lambda$. r_{mn} represents the distance between two atoms m and n. f_m and f_n are the scattering factors of atoms m and n, these being a product of scattering power and a contribution due to thermal vibrations. The scattering power is dependent on Q for X-rays and independent of Q for neutrons, whereas the contribution from thermal vibrations is dependent on Q in both cases. For the case of $m = n$ terms of magnitude f_m^2 result.

The simple form of the DSE results from the assumption that the atoms in a given rigid body are allowed to adopt all orientations in space, as is the case for the atoms in the crystallites of an ideal powder diffraction sample (Warren, 1969). However, the existence of a crystal lattice is not a prerequisite for using the formula. Use of the DSE to model diffraction from crystallites of meaningful size has conventionally required a large computational overhead, since very large numbers of atom pairs enter the sum. Therefore the equation has been applied mainly to glassy systems, for example in the classic work of Warren (1934), where the assumption of spherical symmetry, on average, permitted a reduction to a one-dimensional problem. Over the past 20 years, however, use of the DSE in modelling nanocrystalline systems has become more common. Tettenhorst & Corbató (1988), for example, refer to an execution time of nearly 13 min on an IBM 3081 computer for crystals of boehmite of size 48 × 12 × 48 unit cells. In this connection the term Debye function analysis (DFA) is now routinely employed (Gnutzmann & Vogel, 1990; Hall, 2000; Vogel, 1998). Makinson *et al.* (2000) have used the DSE to model stacking and twin faults in metallic nanocrystals, whereas the work of Pinna (Pinna *et al.*, 2003; Pinna, 2005) has been concerned with inferring the shapes of nanoparticles from X-ray diffraction.

It is shown here that the DSE can also be applied to the diffraction patterns of conventional powders with hundreds of millions of unit cells constituting the coherently scattering domains. It thereby becomes applicable to systems conventionally dealt with by Bragg's law and the Rietveld refinement approach (Rietveld, 1969). Although Grover & McKenzie (2001) took steps in this direction by calculating distance multiplicity functions, their work only considered cubic crystallites explicitly, with dimensions of up to 50 × 50 × 50 unit cells. Furthermore, the method to be defined here contains the

essential element of splitting interatomic pair vectors into lattice and cell contributions.

2. The essence of the new approach

An example of a crystallite is given in Fig. 1, with dimensions $3 \times 4 \times 4$ unit cells.

Vectors joining unit-cell origins may be referred to as lattice-pair vectors, as is always the case in primitive lattices. The length of the vector joining A and B, *i.e.* r_{AB}, can also be calculated *via* an indirect route between atoms A and B, in which vectors between A, B and their respective unit-cell origins are used, as well as lattice-pair vectors [Figs. 1(*a*,*b*)]. It is seen in Figs. 1(*c*) and (*d*) that the vector joining A and B can be regarded as the sum of a lattice-pair vector [−1, −2, 3] and a vector joining points T and B. Since point T corresponds to the centre of atom A translated by the lattice-pair vector, it follows that all interatomic pair vectors can be regarded as the sum of a lattice-pair vector and an interatomic pair vector *referred to a single unit cell* (or Patterson vector). The latter vector is referred to henceforth as a cell-pair vector.

The lattice-pair vectors that arise depend on crystallite size and shape, as does the number of times a given lattice-pair vector occurs. The cell-pair vectors that arise depend on the crystal structure. This rationalization leads to the following re-expression of equation (1), in which the essential means of reducing the computational overhead becomes apparent.

$$I(Q) = \sum_i \sum_{mn,\text{cell}} N_i f_{mn} [\sin(Q|\mathbf{r}_i + \mathbf{r}_{mn}|)/Q|\mathbf{r}_i + \mathbf{r}_{mn}|]. \quad (2)$$

Here the index of summation i represents a lattice-pair vector. The second summation is over atom pairs mn within a single unit cell, and N_i is the number of times lattice-pair vector i occurs within the crystallite. The scattering factors f_m and f_n have been brought together to form a product, *i.e.* $f_{mn} = f_m f_n$. The key to using equation (2) is to know how values of N_i depend on crystallite shape and size. In this work, the assumption is made that the crystallites are parallelepipedal [as in Fig. 1(*a*)], such that their shape and size are defined by the product $L_x L_y L_z$, where L_x, L_y and L_z are the number of unit cells along x, y and z, respectively. In order to calculate the value of N_i for a lattice-pair vector $[n_x, n_y, n_z]$ in a crystallite given by values L_x, L_y, L_z, use is made of equation (3).

$$N(n_x, n_y, n_z) = (L_x - |n_x|)(L_y - |n_y|)(L_z - |n_z|), \quad (3)$$

whereby $0 \leq |n_x| < L_x$, $0 \leq |n_y| < L_y$ and $0 \leq |n_z| < L_z$.

In the particular case of Fig. 2(*a*), for example, where $L_x = 3$, $L_y = 4$ and $L_z = 4$, the equation gives the correct value for $N(-1, -2, 3)$ of $(3 - 1)(4 - 2)(4 - 3) = 2 \times 2 \times 1 = 4$. It has been used earlier by Wilson (1942) and its form may be justified by the following argument. Figs. 2(*b*) and (*c*) refer to one-dimensional 'crystals' for which $L_x = 1$ and 2, respectively. In the first case, $N(0) = 1$, signifying that there is one lattice point only. In the second case $N(0) = 2$, $N(-1) = 1$ and $N(1) = 1$, corresponding to two lattice points, one lattice-pair vector to the left of length 1 and one to the right of length 1. Similarly

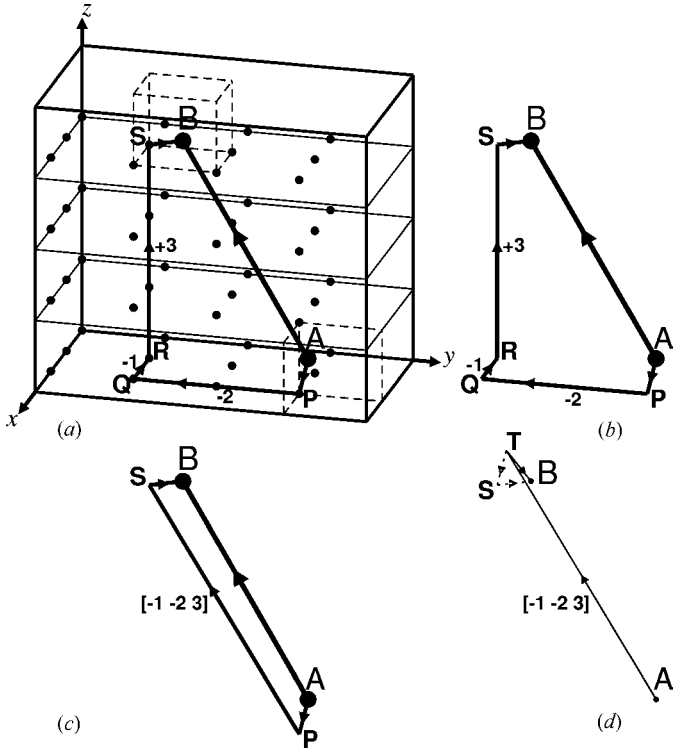

Figure 1
Two atoms A and B and their unit cells, with direct and indirect vector linkages. (*a*) Summary (black dots: origins of unit cells). (*b*) Vectors from (*a*); (*c*) formation of a single lattice-pair vector [−1 ,−2, 3]; (*d*) a change in the order of vector summation, whereby vector **TS** = vector **AP**. **TS** + **SB** = **TB**, a cell-pair vector.

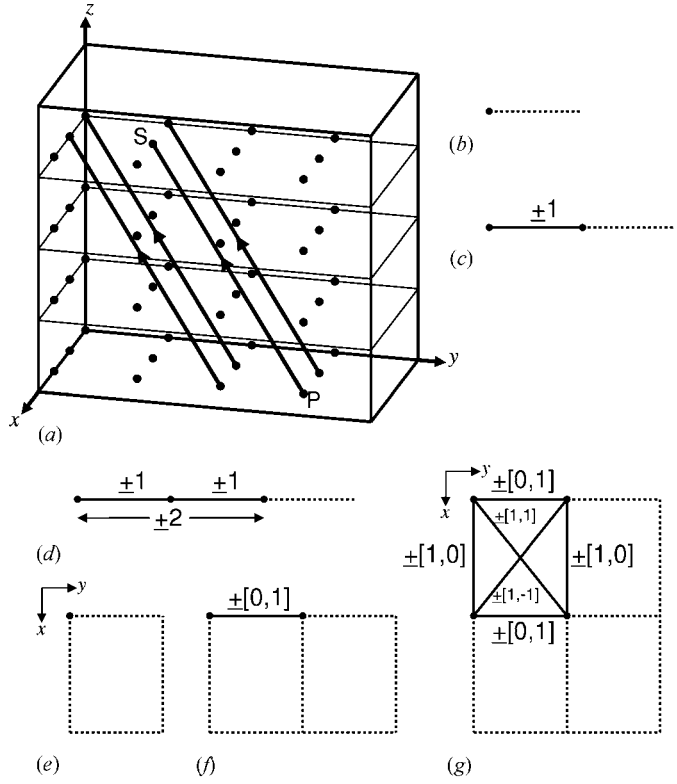

Figure 2
Diagrams relating to the frequencies of lattice-pair vectors for different crystallite sizes.

Table 1
Key to sections in which points A–I are dealt with.

	Points								
System	A	B	C	D	E	F	G	H	I
NaCl	§4.1	§4.2	§4.3	§4.4	§4.5				
PZT			§5.4			§5.1	§5.2	§5.3	
α-Quartz			§6.1	§6.2					
Kaolinite	§7.2	§7.3	§7.4	§7.5					§7.1

for the one-dimensional 'crystal' for which $L_x = 3$ in Fig. 2(*d*), $N(0) = 3$, $N(1) = N(-1) = 2$ and $N(2) = N(-2) = 1$. The results from Figs. 2(*b*)–(*d*) can be summarized by a single result: $N(n_x) = L_x - |n_x|$. It is seen by inspection that the frequencies of lattice-pair vectors in the two-dimensional crystal of Fig. 2(*g*) are given by the following two-dimensional extension: $N(n_x, n_y) = (L_x - |n_x|)(L_y - |n_y|)$. In view of the emerging pattern, the result for a real three-dimensional crystal of dimensions L_x, L_y and L_z is as given above in equation (3).

3. Structure of the article

In the remainder of this article, it is shown how the application of equation (3) allows the computationally efficient calculation of full powder diffraction patterns. The steps required are described by reference to four crystal structures, sodium chloride, lead zirconate titanate (PZT), α-quartz and kaolinite, these belonging to the cubic, monoclinic, trigonal and triclinic crystal systems, respectively. Nine different issues have been identified, as follows. A: cell-pair vectors; B: calculation of pair distribution functions; C: calculation of diffraction patterns; D: influence of crystallite size; E: partial diffraction patterns; F: handling of site-occupancy factors; G: treatment of isotropic atomic displacement parameters; H: treatment of anisotropic atomic displacement parameters; I: structural disorder. These are covered by the four systems as set out in Table 1, in such a way as to allow a logical progression without unnecessary repetition.

Calculated diffraction patterns are shown in order to illustrate these points.

4. Sodium chloride

Structural data for sodium chloride at room temperature and pressure were taken from the article by Walker *et al.* (2004). The single degree of freedom corresponds to the unit-cell parameter, $a = 5.6401$ Å.

4.1. Cell-pair vectors (stage 1)

The set of cell-pair vectors was calculated by constructing a complete unit cell of atoms, such that all atomic coordinates lay in the range $0 \leq x, y, z < 1$. This is necessary for the correct encoding of the approach encapsulated by Fig. 1(*a*). If coordinates outside this range were used, errors in the numbers of interatomic interactions would result. This is because the lattice-pair vectors, which have multipliers governed by equation (3), act as linkages between complete parallelepipedal boxes, with no 'leakage' of atoms between neighbouring boxes allowed. Otherwise the situation would arise that different atoms within the same physical unit cell would be weighted differently in the Debye sum, merely according to the logical unit cell to which they were assigned.

The next step was to calculate the components of the 64 cell-pair vectors formed from the eight atoms in the unit cell, these forming a centrosymmetric set.

4.2. Calculation of pair distribution functions (stage 1)

Although the Debye formalism does not demand the calculation of pair distribution functions (p.d.f.'s), this may be regarded as a convenient intermediate stage for the purposes of this initial work. The calculation proceeds as follows. First a maximum interaction length, $r_{\max}$, is determined from the dimensions of the crystallite. Secondly the length $r_{\max}$ is divided into equally spaced histogram classes, or bins, of width Δr. Thirdly, the population of each bin is set to zero at the start of the calculation. Finally each pair of atoms in the crystallite contributes once to the population of the bin to which it belongs, this being determined by the interaction length.

The calculation of p.d.f.'s also allows a splitting of the Debye calculation into two stages, which is useful here, since the innovative step described in §2 only affects the first stage. In stage 1, the lengths of all the pairwise interactions are calculated, *i.e.* values of $|\mathbf{r}_i + \mathbf{r}_{mn}|$ in equation (2). This results in a p.d.f. for each pair type, *i.e.* Na$\cdots$Na, Na$\cdots$Cl and Cl$\cdots$Cl. In stage 2, diffraction patterns are calculated from the p.d.f.'s, as described in the following sections.

Over the whole Debye sum, as expressed by equations (1) or (2), each pairwise interaction is counted twice: an interaction between atom m in unit cell p and atom n in unit cell q gives rise to the same interaction length as an interaction between atom n in unit cell q and atom m in cell p. However, no new information is conveyed by the second interaction, since only the interaction length is important. Following the splitting of pairwise atomic interactions into lattice- and cell-pair vector contributions, a choice can be made as to whether centrosymmetry is maintained within the set of lattice-pair vectors or within the cell-pair vectors. The decision was taken here to maintain the full set of cell-pair vectors, *i.e.* in an ordered structure, for each vector with components x, y, z there will be a vector with components $-x$, $-y$, $-z$. Consequently only one half of the set of lattice-pair vectors needs to be considered explicitly.

A full set of lattice-pair vectors for a crystallite of dimensions $L_xL_yL_z$ would be given by all combinations of $[n_x, n_y, n_z]$ within the following ranges: $-(L_x - 1) \leq n_x \leq (L_x - 1)$; $-(L_y - 1) \leq n_y \leq (L_y - 1)$; $-(L_z - 1) \leq n_z \leq (L_z - 1)$. Since this set is to be halved, the decision was taken to halve the above z range to $0 \leq n_z \leq (L_z - 1)$. Physically this means that only 'ascending' lattice vectors in Figs. 1(*a*) and 2(*a*) are counted. This halving process requires particular attention when $n_z = 0$, whereby the guiding principle is that no atomic pairwise interaction is to be counted twice. Accordingly

$-(L_x - 1) \leq n_x \leq (L_x - 1)$ but the n_y range is halved: $0 \leq n_y \leq (L_y - 1)$ when $n_x \geq 0$ and $1 \leq n_y \leq (L_y - 1)$ for $n_x < 0$. When $n_x = n_y = n_z = 0$, *i.e.* within a unit cell, each interaction is given a weighting of one half, as a consequence of the centrosymmetry of the set of cell-pair vectors.

Interatomic distances to identify the p.d.f. bin numbers were calculated by a nested loop program structure, with the outer loop proceeding through the set of cell-pair vectors $\mathbf{r}_{mn}$. The three inner loops corresponded to the above required ranges of n_x, n_y and n_z in the lattice-pair vectors $\mathbf{r}_i$. P.d.f. bins were progressively populated in amounts given by equation (3) for the particular n_x, n_y and n_z values. In the course of these calculations, a transformation from fractional to Cartesian coordinates was undertaken by means of standard orthogonalization matrices: cell-pair vectors were transformed prior to the nested-loop structure, whereas lattice-pair vectors were transformed dynamically within the loops, by means of increments in Cartesian space.

The calculation of p.d.f.'s as an intermediate step takes crystal symmetry into account implicitly, in that interactions of equal length are brought together into the same bin. This reduces the computation time in stage 2.

4.3. Calculation of diffraction patterns (stage 2)

4.3.1. The Debye sum expressed in terms of pair distribution functions. The p.d.f. for a given atom pair type s may be expressed as $p_s(j)$, where j is the bin number and p its population. Accordingly the Debye scattering equation now takes on the form

$$I(Q) = \sum_s f_s \sum_j p_s[\sin(Qj\Delta r)/Qj\Delta r]. \quad (4)$$

Here the first summation is over the different pair types and the second over all bins in the corresponding p.d.f. The symbol Δr corresponds to the bin width of the p.d.f., with f_s the product of the scattering factors f_m and f_n of the two atom types making up the pair. Since atomic displacement parameters (ADPs) are required in the stage 2 calculations, a different pair type s must be defined for each different set of ADP values, even when the same two atom types are involved.

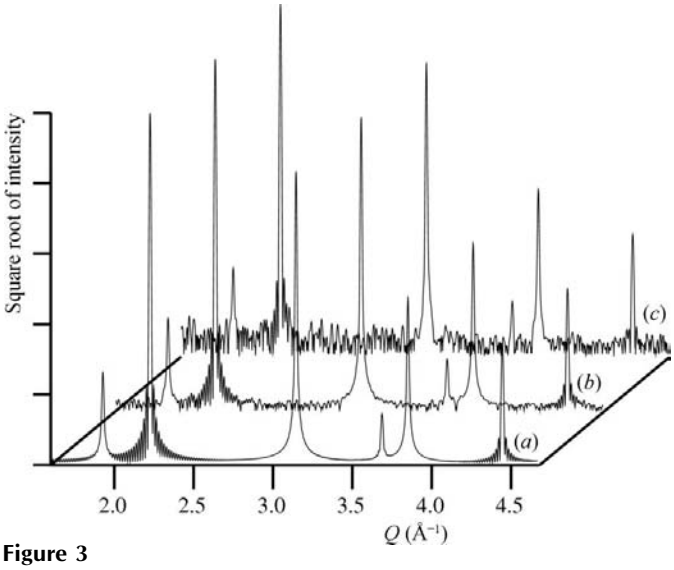

Figure 3
Computed diffraction patterns utilizing X-ray scattering factors for a crystallite of NaCl of dimensions 40 × 40 × 40 nm. (*a*) Exact calculation (without use of p.d.f.); (*b*) with p.d.f. of bin width 0.001 Å; (*c*) with p.d.f. of bin width 0.01 Å.

4.3.2. Choice of *Q* values. A practical computational approach is to consider discrete Q values of constant separation, from which results can be generated for comparison with experiment. The maximum value of Q follows directly from the highest 2θ angle. Ideally the increment ΔQ should be small enough to match the separation of experimental data points at high 2θ values for the radiation component with highest wavelength. For example, with Cu $K\alpha_1/K\alpha_2$ radiation, which has a maximum wavelength of 1.54433 Å, an increment ΔQ equal to 0.001163 Å^{-1} matches a 2θ increment of 0.02° at 70° 2θ.

4.3.3. Atomic scattering factors. The Q-dependent values of atomic scattering factors for X-rays were calculated using

$$f_m(Q) = \sum_{i=1}^{4} a_i \exp(-b_i Q^2/16\pi^2) + c. \quad (5)$$

Values of coefficients a_i, b_i and c for different atom types m were taken from tabulated values in *International Tables for X-ray Crystallography* Volume IV (1974).

Values of the corresponding factors for neutrons, *i.e.* neutron scattering lengths, were taken from the website http://www.ncnr.nist.gov/resources/n-lengths/, these being independent of Q.

4.3.4. Choice of bin width, Δ*r* and computation of *I*(*Q*). Just as discrete Q values are taken, so discrete values of pairwise interatomic separation are used, with an accuracy determined by the bin width of the p.d.f. Although this width does not significantly affect computation times in stage 1 (*i.e.* calculation of p.d.f.'s), smaller values of Δr necessarily lead to longer computation times in stage 2, at which $I(Q)$ is calculated. As it is anticipated that an improved method will be developed in future, whereby p.d.f.'s will not be used, the decision was taken to employ a direct method for calculating $I(Q)$. Thus computational speed was not a major consideration in stage 2, in comparison to stage 1. With respect to $I(Q)$, a fixed array of 640 000 equally spaced values of $\sin\theta$ was calculated, spanning the principal range $0 < \theta \leq 2\pi$. Calculated values of the product Qr (in allowed discrete intervals of $\Delta Q \Delta r$) were mapped into the principal range, thereby accessing the appropriate element of the $\sin\theta$ array and exploiting the periodicity of this function.

Since Pinna (2005) has highlighted the errors arising in the p.d.f. method through the representation of interatomic distances as histogram classes of finite width (bin numbers), an investigation was carried out of the influence of bin width on the calculated diffraction pattern (Fig. 3). The convention has been adopted here, and in several subsequent figures, of plotting the square root of intensity, in order to provide more detail on the shapes of weaker maxima. The units of intensity are defined in §4.3.5.

In the exact calculation, which was carried out as a reference, the exact distances between atom pairs were stored at the end of stage 1, rather than the numbers of atom pairs in different bins of discrete width. The significant features of the pattern in Fig. 3(*b*), for which a bin width of 0.001 Å was used, are in good agreement with the exact pattern of Fig. 3(*a*). By comparison, the pattern of Fig. 3(*c*), to which a bin width of 0.01 Å applies, is characterized by significant noise in the background. As a consequence, the decision was taken to utilize bin widths of 0.001 Å for the diffraction patterns generated in this article, in anticipation that the use of p.d.f.'s will be superseded in future work. Note that the bases of the two peaks at approximate Q values of 2.22 and 4.45 Å^{-1} show an oscillatory character, which is due to the finite crystallite size.

4.3.5. Scaling of intensities. Although there is no need to apply absorption corrections for the purposes of this work, the dependence of the calculated intensity on crystallite size is relevant. The basic consideration here is to assume that the same volume of sample is irradiated, irrespective of crystallite size. Further, a random orientation of crystallites is assumed. Consequently, the smaller the crystallite volume, the greater the number of crystallites that will be correctly oriented for a diffracted signal to be detected. Thus the intensity calculated from a given crystallite should be scaled by a factor inversely proportional to its volume. Since equation (3) can also be written as $N(n_x, n_y, n_z) = L_xL_yL_z(1 - |n_x|/L_x)(1 - |n_y|/L_y)(1 - |n_z|/L_z)$, and crystallite volume is equal to $V_{uc}L_xL_yL_z$, with V_{uc} the unit-cell volume, bin populations were calculated by using the factor $(1 - |n_x|/L_x)(1 - |n_y|/L_y)(1 - |n_z|/L_z)$. A multiplying factor of $1/[N_{uc}V_{uc}]$, with N_{uc} the number of atoms in the unit cell, was subsequently applied at the end of stage 2. This procedure gives rise to intensities per atom (in electronic units), which apply across all crystallite sizes.

The decision was taken not to apply a Lorentz–polarization factor, as this is often routinely taken into account by the software associated with modern diffractometers.

4.3.6. Conversion from Q to 2θ values. Since $Q = 4\pi \sin\theta/\lambda$, $2\theta = 2\arcsin(Q\lambda/4\pi)$. Since the intensities are calculated at discrete, equally spaced Q values, the mapping into equally spaced 2θ angles is carried out by a process of interpolation. A further consideration is the relative weighting of the $K\alpha_1$ and $K\alpha_2$ intensities, which was taken as 2:1 in this work.

4.4. Influence of crystallite size

X-ray diffraction patterns of NaCl are given in Fig. 4, without temperature-factor corrections, for ten nominal crystallite sizes.

Since number of unit cells is an integer, the real dimensions will deviate from these nominal values. For example, the 20^3 nm^3 sample corresponds to a cluster of $35 \times 35 \times 35$ unit cells, of true dimensions 19.74035^3 nm^3. The largest sample, of volume 200^3 nm^3, corresponds to a linear dimension of 0.2 µm, this being a typical coherence length for a conventional powder in the micron range.

In Figs. 4(*a*,*b*) the maxima become successively taller and narrower as the crystallite dimension is increased in the range between 20 and 100 nm. The observed jaggedness in some maxima is a consequence of the finite increment in 2θ of 0.02°, as is also the case for most commercial diffractometers. For larger crystallite sizes between 120 and 200 nm [Figs. 4(*c*,*d*)], the predominant effect is no longer peak narrowing, although this still takes place, but a separation of the maxima due to Cu $K\alpha_1$ and Cu $K\alpha_2$ radiation.

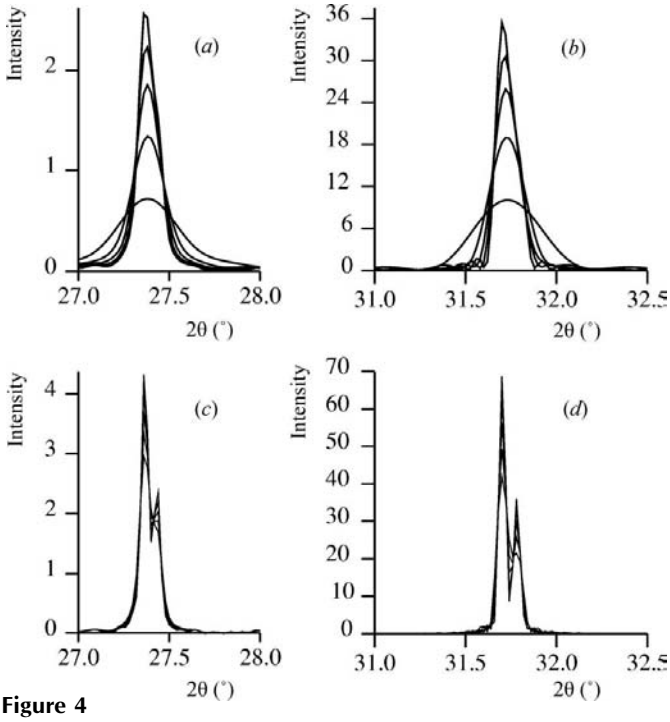

Figure 4
Computed diffraction patterns in the regions of the first and second maxima for NaCl, for Cu $K\alpha_1/K\alpha_2$ radiation. (*a*,*b*) Cubic crystallites of lengths 20, 40, 60, 80 and 100 nm; (*c*,*d*) cubic crystallites of lengths 120, 140, 160, 180 and 200 nm.

4.5. Partial diffraction patterns

Owing to the linearity of the Debye sum, it is possible to subdivide it into contributions from different types of atom pairs (Fig. 5).

The emergence of two sharp minima is to be noted, with intensities below the background level in the partial diffraction pattern of Na···Cl atom pairs, at angles of 27.4 and 53.9° 2θ, respectively. These correspond to the {111} and {311} reflections in a conventional indexing of the pattern, for which indices h, k and l are all odd. The other Na···Cl reflections, with all even indices, are associated with maxima.

5. Lead zirconate titanate

A monoclinic structural model of the perovskite system $Pb(Zr_{0.54}Ti_{0.46})O_3$ (PZT) was selected (Frantti *et al.*, 2000) in order to illustrate further aspects of the approach. The continued investigation of this ceramic is of technological significance because of its widespread use as a piezoelectric actuator and sensor. The unit cell proposed is a = 5.76907, b =

5.74266 and c = 4.08900 Å, with β =90.4968°. Zirconium and titanium ions are disordered over the octahedrally coordinated B sites, whereby the model assigns different coordinates to the Zi^{4+} and Ti^{4+} ions, this representing a difficulty for the DSE approach to deal with. Anisotropic atomic displacement parameters are assigned to the lead and oxygen ions, whereas the thermal motion of the B-site ions is represented by isotropic displacement parameters.

5.1. Handling of site-occupancy factors

A p.d.f. essentially conveys information concerning the coordinates of different atomic sites within the crystallite. Thus the existence of two or more atoms at a particular atomic site, each with fractional occupancy factors, was handled by defining a single, complex atom made up of contributing atoms in proportion to their occupancy factors. In cases where the total occupancy of a site was less than one, as in this PZT system, a vacancy was assigned to the non-occupied proportion of the site. P.d.f.'s were calculated in stage 1 assuming total occupancies of one on all sites, with the identities of the complex atoms carried over into stage 2 in order to calculate the diffraction patterns.

Two difficulties arise from this approach. First it is possible that close contacts are generated between atomic sites that are fractionally occupied. This was the case in this system, where erroneous contacts of length 0.247 Å were generated between Ti^{4+} and Zr^{4+} ions. These can be dealt with by straightforward elimination from the relevant p.d.f. Secondly, special handling is required for pairwise atomic interactions of length zero when complex atoms are involved, since it is a physical impossibility for two or more different atom types, or for an atom and a vacancy to occupy a single atomic site. Consider a case of atoms m and n contributing to a complex atom in the proportions of their occupancy factors SOF(m) and SOF(n). For all interactions of non-zero length, the contribution to the diffracted intensity scales as $f_m f_n$ SOF(m) SOF(n), where f_m, f_n are the atomic scattering factors of m and n. Although this result would also accidentally apply to interactions of zero length when $m = n$ and SOF(m) = 1, the total contribution to the diffraction pattern for identical m and n of interaction length zero has the fundamental form $N_{uc}[\mathrm{SOF}(m) f_m^2]$. Here N_{uc} is the number of unit cells in the crystallite.

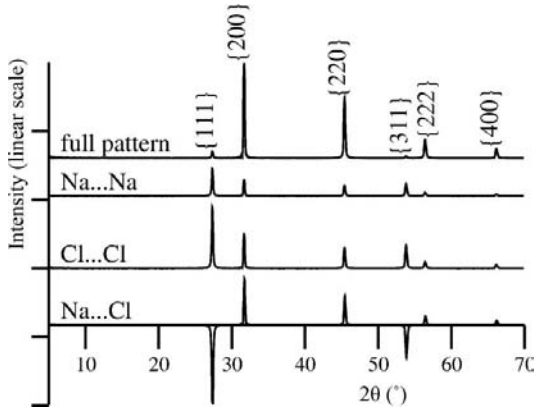

Figure 5
The full diffraction pattern for NaCl (Cu $K\alpha_1/K\alpha_2$ radiation; crystallite dimension 40 nm) as a linear superposition of partial diffraction patterns for Na···Na, Cl···Cl and Na···Cl atom pairs.

5.2. Treatment of isotropic atomic displacement parameters

The proposed model for PZT contains isotropic atomic displacement parameters for the titanium and zirconium atoms, U_{iso}, with anisotropic displacement parameters for the other three atom types. The standard Debye–Waller factor, when expressed in terms of the parameter Q, takes on the form

$$T(Q) = \exp\left(8\pi^2 U_{iso} \sin^2\theta/\lambda^2\right) = \exp\left(-U_{iso} Q^2/2\right). \quad (6)$$

This factor was used to calculate temperature-modified atomic scattering factors $f_m(Q)T(Q)$ in stage 2, with $f_m(Q)$ calculated according to equation (5).

5.3. Treatment of anisotropic atomic displacement parameters

A full treatment of anisotropic displacement parameters (ADPs) is problematical for the current method, since directional information is lost when p.d.f.'s are calculated as an intermediate stage. This difficulty could be circumvented by storing the effects of the Gaussian broadening of the pairwise atomic interaction distances as modified bin occupancies in the p.d.f.'s.[1] However, this option was not adopted, since the increase in computational time can not be justified by the benefit. Furthermore, as the use of p.d.f.'s as an intermediate stage will be discarded in future work, this effort is not essential here. Instead a curtailed treatment of ADPs was carried out, in that equivalent isotropic temperature factors were derived. As described by Trueblood *et al.* (1996), ADP tensors (whether in $\boldsymbol{\beta}^{ij}$, $\boldsymbol{U}^{ij}$ or $\boldsymbol{B}^{ij}$ notation) can be converted routinely to equivalent isotropic ADPs, U_{eq}, for substitution into equation (5) during stage 2 of the calculation. Thus the loss of directional information brought about by the use of p.d.f.'s was partly circumvented by a method requiring very little extra computational overhead.

5.4. Calculation of diffraction patterns

The structural model of PZT proposed by Frantti *et al.* (2000) led to there being five effective atom types [Pb, Zr, Ti, O(ADP 1), O(ADP 2)] and so 15 different pair types (5 + 4 + 3 + 2 + 1). Whereas stage 1 of the calculation could be carried out relatively rapidly, the execution times for stage 2 were considerably longer, mainly as a consequence of there being 15 separate p.d.f.'s (see §8.2). This also points to the need to develop a single-stage calculation in future. The results are given in Fig. 6.

Peak positions are in agreement with the *hkl* reflections generated from the unit-cell parameters, as demonstrated at

[1] The method would require a calculation of the eigenvectors and eigenvalues of the ADP tensor, followed by a calculation of the mean-squared displacement along the interatomic vector, utilizing an equation proposed by Nelmes (1969).

higher magnification for the cluster of maxima at approximately 55° 2θ in Figs. 7(*a*,*b*). The advantage of losing the Cu $K\alpha$ peak splitting by utilizing neutrons of wavelength 1.47 Å is also seen.

6. Quartz

Since quartz is extremely widespread as a mineral present in ceramic raw materials such as plastic clays and raw kaolins, its presence and concentration are frequently monitored by X-ray diffraction. The structural model taken as the basis of the calculations here was proposed by Kihara (1990). This refers to a single crystal of natural left-handed α-quartz of trigonal symmetry in space group $P3_221$, for which X-ray data were collected at room temperature and pressure.

6.1. Calculation of diffraction patterns

Seventy-four different cell-pair vectors were generated from the nine atoms in the rhombohedral cell with hexagonal axes, with two different sets of ADPs utilized at the outset, one for silicon and the other for oxygen atoms. Accordingly there are only three atom-pair types, Si···Si, Si···O and O···O.

6.2. Influence of crystallite size

The question of particle size is of importance when selecting ceramic raw materials. Accordingly attention is paid to this here by generating X-ray diffraction patterns of quartz with crystallite lengths of 40, 80, 120, 160 and 200 nm. Owing to the geometry of the unit cell, the resulting crystallites had a prismatic habit, with clusters of size ranging from 81 × 81 × 74 to 407 × 407 × 370 unit cells.

Calculated diffraction patterns for the five different crystallites are given in Fig. 8. It is directly seen how increasing crystallite size leads to narrower and higher maxima.

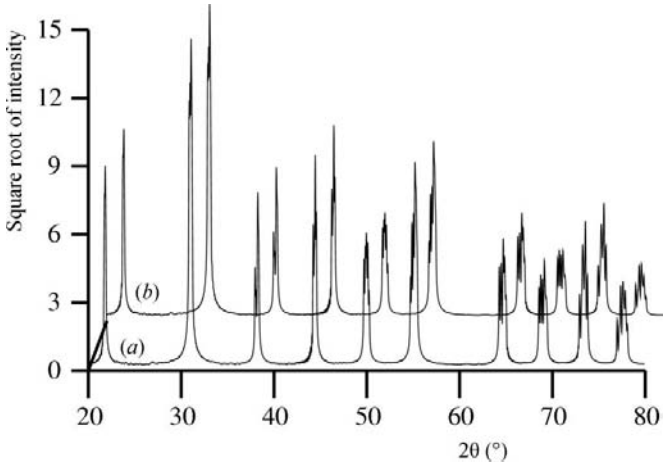

Figure 6
Computed diffraction patterns for crystallites of PZT of dimension 100 × 100 × 100 nm with Cu $K\alpha_1/K\alpha_2$ radiation (*a*) without atomic displacement parameters; (*b*) with isotropic and equivalent isotropic atomic displacement parameters.

Also of interest is the development of the characteristic feature of the 'five fingers of quartz' as the crystallite size increases (Fig. 9*a*), this being a commonly used test for diffractometer alignment. The five fingers cannot be resolved at the smallest crystallite length of 40 nm. The common industrial practice of utilizing the $\{2\bar{1}2\}$ reflection at 50.2° 2θ to calculate quartz concentration is indicated in Fig. 9(*b*). This has the advantage of there being no overlaps with reflections from other common minerals, such as feldspars and clay minerals. The total areas under the computed curves between the 2θ angles of 49.00 and 51.50° are listed in Table 2.

In summary, the area is relatively invariant to crystallite size, as is commonly known. The mean area is equal to 0.7039°, with an r.m.s. deviation of 0.80%, the latter value being consistent with the error normally associated with this test method.

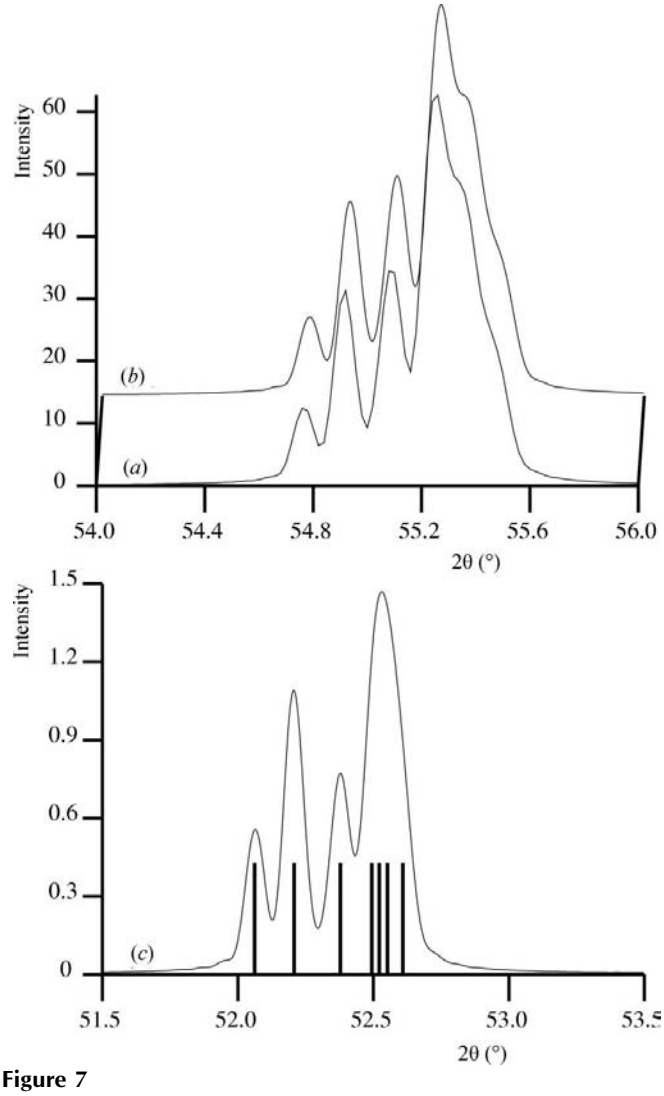

Figure 7
(*a*) Magnification of Fig. 6(*b*) in the 2θ range from 54 to 56°; (*b*) as (*a*), but with a 2θ resolution of 0.002° instead of 0.02°; (*c*) calculated diffraction pattern due to the same *hkl* planes for neutrons of wavelength 1.47 Å. The vertical bars indicate the maxima for *hkl* values in the forms $\{20\bar{2}\}$, $\{31\bar{1}\}$, {022}, $\{13\bar{1}\}$, {202}, {311} and {131}, from left to right, as calculated from the unit-cell parameters (2θ resolution 0.005°).

7. Kaolinite

Just as quartz is present in many ceramic raw materials, kaolinite is a very important mineral within the clay mineral fraction. However its quantitative determination by X-ray diffraction is difficult because of three factors: first, the predominance of fine particles in the equivalent spherical diameter fraction < 0.2 μm, secondly the widespread occurrence of structural disorder, and thirdly the occurrence of preferred orientations in the powder sample. The first two factors can be handled directly by the DSE method, with the third capable, in principle, of being treated by a subsequent correction.

The crystal structure model proposed by Bish (1993) was used as a basis for the calculations here. This was derived from a low-temperature (1.5 K) powder neutron study of a composite sample taken from several geodes of Keokuk, Iowa kaolinite. The low-symmetry, triclinic space group *C*1 was adopted, with isotropic temperature factors quoted for Al, Si and O atoms and anisotropic factors given for the H atoms. In view of the low temperature to which the data apply, it is anticipated that the high-angle intensities will be somewhat larger than is the case at room temperature. However, the data allow the potential of the new DSE approach to be evaluated in modelling structural disorder. In essence the aim is to maintain the computational advantage introduced by the cellular method [as encapsulated by equation (3)] without losing the powerful generality of the DSE itself in being able to calculate the diffraction patterns of *all* solid-state structures.

7.1. Structural disorder

Mechanisms of structural disorder in kaolinites have been examined by Artioli *et al.* (1995) and their corresponding diffraction patterns calculated with *DIFFaX* (Treacy *et al.*, 1991), a computer program which is able to model the presence of planar faults. The simplest model of kaolinite disorder is used in the present work, which goes back to the model of Plançon & Tchoubar (1975), where shifts between the 1:1 layers of 0, +**b**/3, −**b**/3 are allowed.

Table 2
Total areas under the split $\{2\bar{1}2\}$ reflection for different crystallite lengths.

Increment in $2\theta = 0.02^\circ$.

Crystallite length (nm)	Area (°)
40	0.6931
80	0.7037
120	0.7068
160	0.7080
200	0.7079

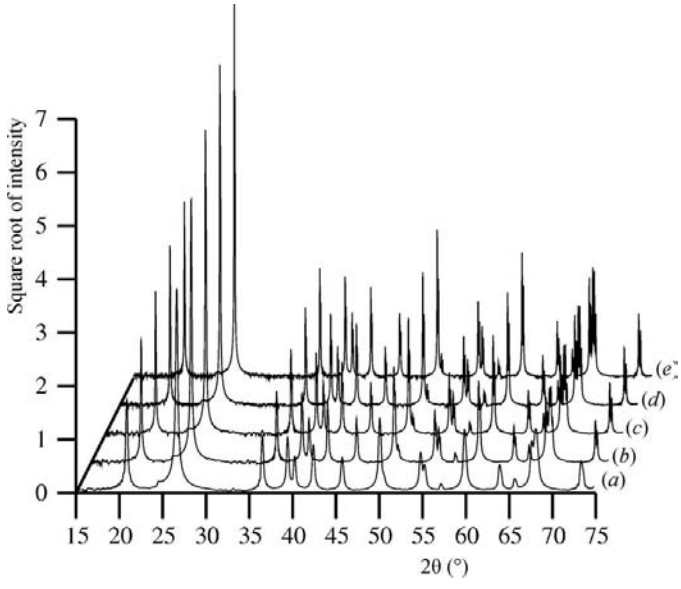

Figure 8
Calculated diffraction patterns of quartz (Cu $K\alpha_1/K\alpha_2$ radiation) for five different crystallite lengths: (*a*) 40 nm; (*b*) 80 nm; (*c*) 120 nm; (*d*) 160 nm; (*e*) 200 nm.

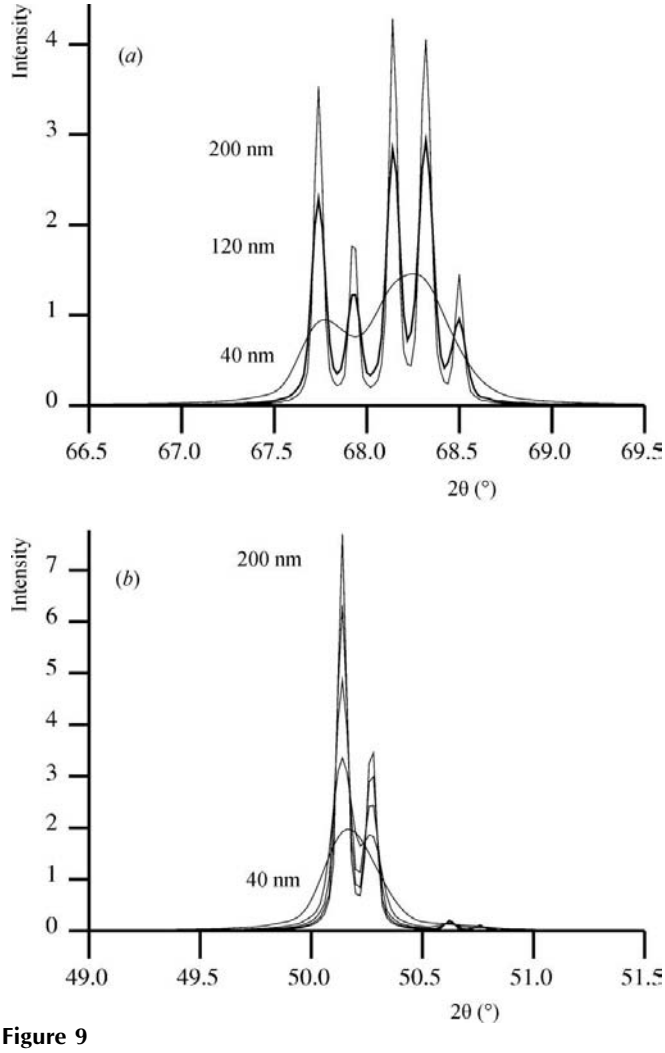

Figure 9
(*a*) Development of the five fingers of quartz for Cu $K\alpha_1/K\alpha_2$ radiation, as a result of the splitting of the $\{3\bar{2}2\}$, $\{2\bar{2}3\}$ and $\{3\bar{3}1\}$ reflections, as shown for crystallite lengths of 40, 120 (thick line) and 200 nm. (*b*) Use of the $\{2\bar{1}2\}$ reflection to quantify quartz concentrations in ceramic raw materials, as shown for five crystallite lengths of 40, 80, 120, 160 and 200 nm.

Table 3
Absolute layer displacements for 1:1 layers 0 to 10, corresponding to a given sequence of random numbers.

The displacements generated depend on φ_{dis}.

L	p	$\varphi_{dis} = 0$ $p_1 = 1.0000$ $p_2 = 1.0000$ Absolute layer displacement	$\varphi_{dis} = 0.25$ $p_1 = 0.8333$ $p_2 = 0.9167$	$\varphi_{dis} = 0.5$ $p_1 = 0.6667$ $p_2 = 0.8333$	$\varphi_{dis} = 0.75$ $p_1 = 0.5000$ $p_2 = 0.7500$	$\varphi_{dis} = 1$ $p_1 = 0.3333$ $p_2 = 0.6667$
10	0.7158	0	+**b**/3	−**b**/3	+**b**/3	0
9	0.2772	0	+**b**/3	+**b**/3	0	+**b**/3
8	0.9316	0	+**b**/3	+**b**/3	0	+**b**/3
7	0.2575	0	−**b**/3	−**b**/3	+**b**/3	−**b**/3
6	0.8910	0	−**b**/3	−**b**/3	+**b**/3	−**b**/3
5	0.6316	0	+**b**/3	0	−**b**/3	0
4	0.5342	0	+**b**/3	0	+**b**/3	−**b**/3
3	0.8744	0	+**b**/3	0	0	+**b**/3
2	0.0330	0	0	+**b**/3	+**b**/3	−**b**/3
1	0.7151	0	0	+**b**/3	+**b**/3	−**b**/3
0	Start:	0	0	0	0	0

Table 4
Frequencies of occurrence, n, together with corresponding weights $w(n_z, 0.5)$ for the layer sequence of the $\varphi_{dis} = 0.5$ structure in Table 3.

$n_z = \Delta L$, the difference in L between a pair of atomic layers in Table 3.

n_z	$n(0)$	$n(+\mathbf{b}/3)$	$n(-\mathbf{b}/3)$	$w_1(n_z, 0.5)$	$w_2(n_z, 0.5)$	$w_3(n_z, 0.5)$
10	0	0	1	0.0000	0.0000	1.0000
9	0	2	0	0.0000	1.0000	0.0000
8	1	2	0	0.3333	0.6667	0.0000
7	2	0	2	0.5000	0.0000	0.5000
6	1	2	2	0.2000	0.4000	0.4000
5	1	4	1	0.1667	0.6667	0.1667
4	2	3	2	0.2857	0.4286	0.2857
3	2	1	5	0.2500	0.1250	0.6250
2	1	2	6	0.1111	0.2222	0.6667
1	5	2	3	0.5000	0.2000	0.3000
0	11	0	0	1.0000	0.0000	0.0000

A more general definition of the lattice-pair vectors introduced in §2 is now required. Accordingly, these vectors still link space-filling parallelepipedal cells, but these cells are no longer constrained to be identical to one another. Thus equation (3) is replaced by three equations, one for each type of interlayer shift, k.

$$N_k(n_x, n_y, n_z) = (L_x - |n_x|)(L_y - |n_y|)(L_z - |n_z|)w_k(n_z, \varphi_{dis}). \quad (7)$$

Here $w_k(n_z, \varphi_{dis})$ is the weighting, or the relative contribution made by layer pairs with shift-type k to the p.d.f. This weighting will depend on the value of n_z and the degree of disorder, φ_{dis}, a parameter which is allowed to vary between zero and one. In the case of disordered kaolinite, k is equal to one for a relative layer shift of zero, two for a relative layer shift of +**b**/3 and three for a relative layer shift of −**b**/3, such that $w_1 + w_2 + w_3 = 1$.

As described in §4.2, n_z values are constrained to be zero or positive. For a fully ordered structure, all weights for $k = 1$ are equal to one, whereas all weights for $k = 2$ or $k = 3$ are equal to zero. For a fully disordered structure, all weights for $n_z \neq 0$ are equal to 1/3, whereas $k = 1$ weights for $n_z = 0$ are equal to one, with $k = 2$ and $k = 3$ weights for $n_z = 0$ equal to zero. This reflects the impossibility of a relative layer shift within a layer. This situation may be summarized as follows: $w_1(n_z, 0) = 1$, $w_2(n_z, 0) = 0$, $w_3(n_z, 0) = 0$ (fully ordered); $w_1(0, 1) = 1$, $w_2(0, 1) = 0$, $w_3(0, 1) = 0$, $w_k(n_z \neq 0, 1) = 1/3$ (fully disordered).

The parameter φ_{dis} may be regarded as a continuous variable with values between 0 and 1. However, the analytical derivation of the weights for intermediate degrees of disorder, *i.e.* $0 < \varphi_{dis} < 1$, is not straightforward. Consequently a random-number generator was employed to generate concrete sequences of layers, from which the weights could be derived. Since a sequence of real numbers p between 0 and 1 is generated, two critical values, p_1 and p_2, were defined in order to define value ranges to which different relative layer shifts apply. These depend on φ_{dis} as follows.

$$p_1 = 1 - 2\varphi_{dis}/3; \quad p_2 = 1 - \varphi_{dis}/3. \quad (8)$$

These criteria were applied by carrying out up to three tests. Test 1 is carried out first, with test 2 only applied if test 1 fails. Similarly test 3 is only carried out if test 2 fails.

$$\begin{aligned} &\text{Test 1: } 0 \leq p \leq p_1\text{: relative shift } 0,\\ &\text{Test 2: } p_1 < p \leq p_2\text{: relative shift } +\mathbf{b}/3,\\ &\text{Test 3: } p_2 < p \leq 1\text{: relative shift } -\mathbf{b}/3. \end{aligned} \quad (9)$$

A sequence of ten random numbers p is given in Table 3 for illustrative purposes. Proceeding from the bottom of the table to the top, the absolute displacements result from the relative shifts between adjacent layers. These in turn are generated from the p values, whereby their interpretation depends on critical values p_1 and p_2.

The values in Table 3 are now used to determine the number of times different relative shifts arise for the various values of φ_{dis}. This process is summarized in Table 4, where the case of $\varphi_{dis} = 0.5$ has been taken as an example.

7.2. Cell-pair vectors

The existence of three different relative layer shifts is handled by generating three different unit cells, which may be labelled A, B and C. A is a normal unit cell, *i.e.* one where all atoms have absolute displacements of zero. B is a cell where the y coordinates of all atoms are displaced by +1/3 and C is a cell in which the y coordinates of all atoms are displaced by −1/3. Three different sets of cell-pair vectors are generated, corresponding to k values 1, 2 and 3. A relative shift of zero is modelled (*i.e.* $k = 1$) by generating the set of cell-pair vectors resulting from pairing an A cell with itself, as in an ordered structure. Relative layer shifts of +**b**/3 ($k = 2$) and −**b**/3 ($k = 3$) are modelled by generating the sets of cell-pair vectors resulting from cell A–cell B and cell A–cell C pairs, respectively.

7.3. Calculation of pair distribution functions

The generation of p.d.f.'s is controlled by equation (7), with weights w_k derived from the results of the random-number generator, as described in §7.1. The appropriate set of cell-pair vectors is used for a given value of k.

7.4. Calculation of diffraction patterns

Since the p.d.f.'s contain all the information relating to structural disorder and crystallite size, X-ray diffraction patterns are calculated as described in §4.3. In order to reduce computation times, atomic pair interactions involving the weakly scattering H atoms were disregarded. Results indicative of the influence of structural disorder were generated by considering crystallites with dimensions of 200 nm in the x and y directions and 20 nm in the z direction, thereby implying the well known platy morphology of kaolinite. The resulting clusters consisted of 388 cells in the x direction, 223 in the y direction and 27 in the z direction. The result obtained for fully ordered kaolinite is given in Fig. 10(a).

Noticeable here are the oscillations in the diffraction pattern from 5° 2θ up to the first maximum at 12.4°, the latter corresponding to the basal 001 reflection. In order to investigate whether these could be suppressed, a lower Δr resolution was adopted for Fig. 10(b), although no significant changes are observed. Since the diffraction patterns in Figs. 10(a,b) are qualitatively similar, the lower resolution was adopted for the rest of the kaolinite work, in order to reduce computation times at stage 2. It was subsequently concluded that these oscillations are due to the shorter crystallite length along the z axis, since the adoption of an equidimensional crystallite for Fig. 10(c) led to their disappearance.

Diffraction patterns for fully disordered kaolinite, *i.e.* for $\varphi_{dis} = 1$, were calculated both analytically, using the weights described in §7.1, and by means of a random-number generator (Fig. 11). Whereas there is complete agreement in the region of the 001 reflection at 12.4°, the curve associated with the random-number generator is considerably noisier compared to the underlying smooth, analytically generated curve. This observation points to the weakness of the random-number approach in its raw form. The sequence of random numbers applies to a single crystallite, which is assumed to be repeated in random orientation throughout the whole sample. In practice, the arbitrariness of the random numbers used within this single crystallite will lead to varying results, such that an average diffraction pattern based on many random sequences should really be generated. In the limit, this averaging process would generate identical weights to the analytical approach. Alternatively, the weights for the different layer shifts for cases of intermediate disorder ($0 < \varphi_{dis} < 1$) could be calculated analytically using a 'probability tree'. The resolution of these issues is reserved for future work.

The two predominant effects of complete disorder are the disappearance of many reflections, together with a general increase in the background level of the diffraction patterns.

The capability of the method to calculate diffraction patterns for intermediate degrees of disorder ($\varphi_{dis} = 0.25, 0.50, 0.75$) is shown in Fig. 12, with the understanding that the random-number-generator-based calculation of the weights will give rise to noisy curves. As expected, basal reflections 001

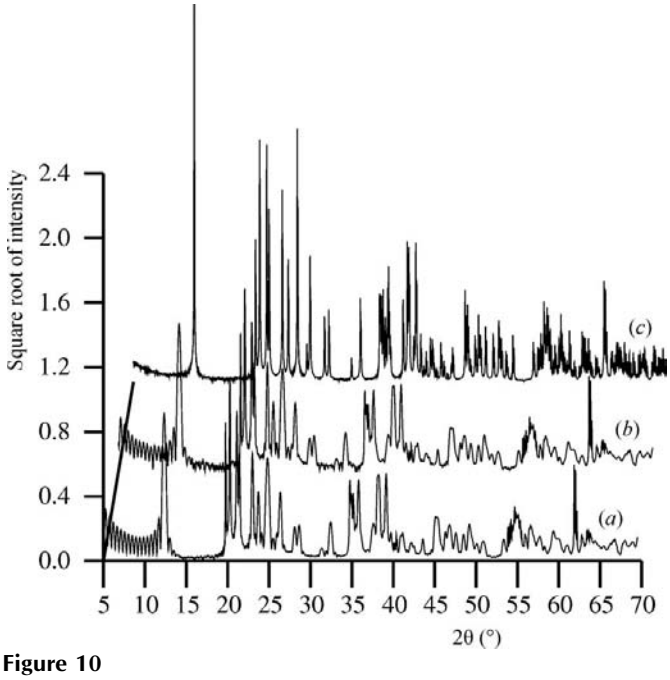

Figure 10
Calculated X-ray diffraction patterns of fully ordered kaolinite ($\varphi_{dis} = 0$) for Cu $K\alpha_1/K\alpha_2$ radiation. (a) Crystallite of dimensions 200 × 200 × 20 nm with $\Delta r = 0.001$ Å; (b) as (a), but with $\Delta r = 0.01$ Å; (c) crystallite of dimensions 200 × 200 × 200 nm with $\Delta r = 0.001$ Å.

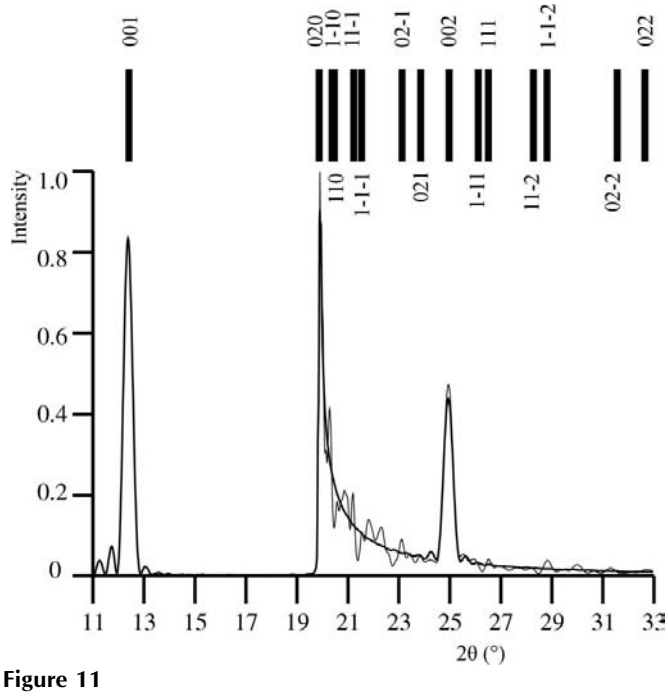

Figure 11
Computed diffraction patterns for crystallites of disordered kaolinite ($\varphi_{dis} = 1$) of dimension 200 × 200 × 20 nm in a significant diffraction range (Cu $K\alpha_1/K\alpha_2$ radiation). Smooth curve: analytically generated; noisier curve: obtained with a random-number generator. The angles of reflections in ordered kaolinite are shown as a comparison.

and 002 (at 2θ angles of 12.4 and 24.9°) have identical heights-over-background in all five patterns. A progressive disappearance of reflections in the region between 20 and 30° 2θ is observed as φ_{dis} increases from 0 to 1.

7.5. Influence of crystallite size

The question of particle-size distribution is of primary importance for an understanding of the ceramic properties of clays, in particular their plasticity and suitability for different forming processes. Fig. 13 shows a sequence of diffraction patterns calculated for geometrically similar platelets of aspect ratio 1:10.

Three reflections are highlighted because of their particular interest, *i.e.* 001 at 12.4° 2θ, 002 at 25.0° 2θ and 060 at 62.3° 2θ. The intensities of the first two basal reflections disappear completely at the smallest crystallite size, with considerable peak smearing also observed in the d = 40 crystallite. With respect to the high-angle 060 reflection, a considerable reduction in intensity is observed with decreasing particle size.

It is to be noted how a wedge shape is generated in Fig. 13(*a*) between 19 and 30° 2θ, which is similar in profile to that of disordered kaolinite in Fig. 11. However this is merely due to a reduction in particle size and is not connected with disorder. The key symptom for a size effect is the reduction in intensity of the 002 reflection, which lies within this angle range. Such a reduction is not observed in completely disordered kaolinite [see Figs. 11 and 12(*e*)]. The basis for a re-evaluation of the X-ray diffraction patterns of kaolinite-containing clays has thus been created.

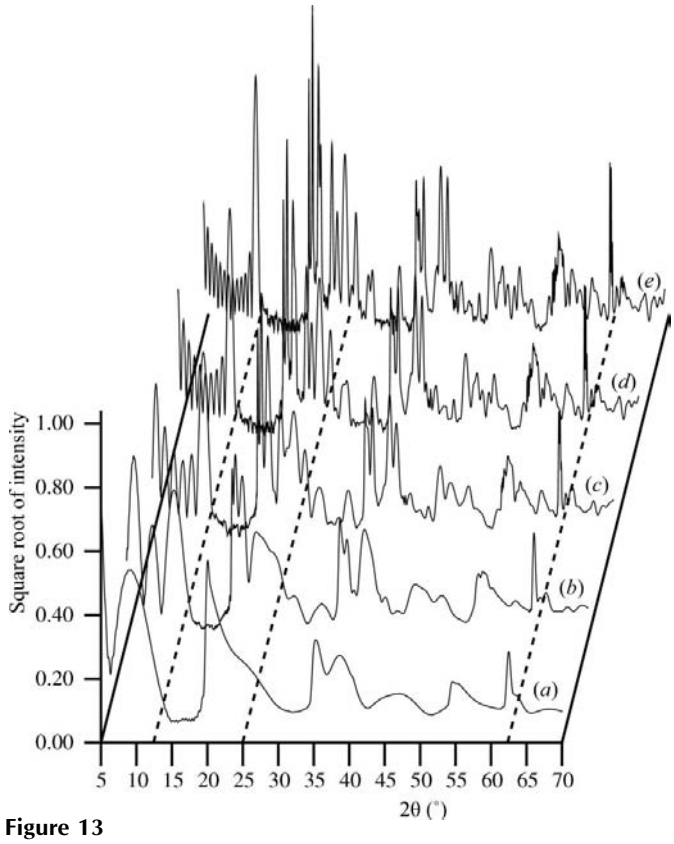

Figure 13
The dependence of diffraction pattern on crystallite size, as seen for a series of platelets of dimensions $d \times d \times d/10$ nm of ordered kaolinite (Cu $K\alpha_1/K\alpha_2$ radiation). (*a*) d = 20; (*b*) d = 40; (*c*) d = 80; (*d*) d = 120; (*e*) d = 160. The intensities of the three reflections linked by the dashed lines are particularly sensitive to crystallite size.

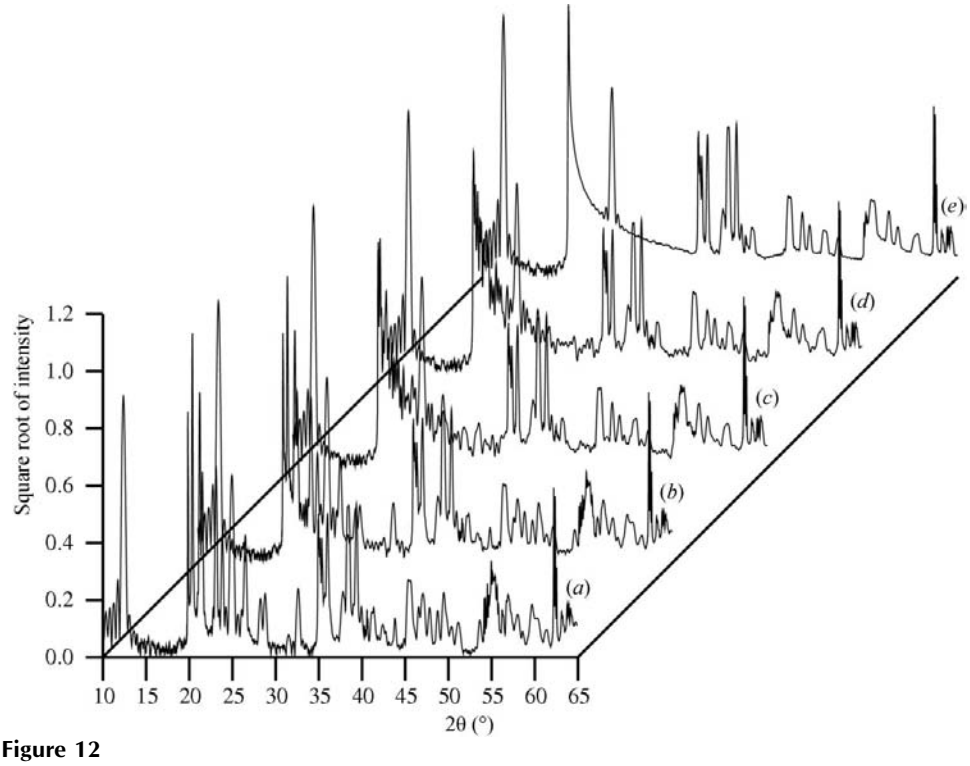

Figure 12
Calculated diffraction patterns (Cu $K\alpha_1/K\alpha_2$ radiation) for a crystallite of kaolinite of dimensions 200 × 200 × 20 nm, for the following values of φ_{dis}: (*a*) 0.00; (*b*) 0.25; (*c*) 0.50; (*d*) 0.75; (*e*) 1.00.

8. Discussion

8.1. Summary of progress made

The essential step in this work has been to make a splitting of pairwise atomic interactions into two parts, a lattice-pair vector and a cell-pair vector part. Separate treatment of lattice-pair vectors made possible the application of equations (3) and, more generally, (7). This brought about a saving in computation time sufficient to allow the DSE to be applied to crystallites of conventional, *i.e.* non-nanoparticle, size, for which the relevant upper length value for diffraction is also influenced by the coherence length of the radiation. The treatment of the cell-pair vector part has been developed sufficiently to indicate how disordered crystalline systems can be modelled with the DSE, whilst

maintaining the formalism of equation (7). The ability of the Debye approach to generate diffraction patterns with full backgrounds and complex peak profiles has been demonstrated, without the need to specify idealized, parameterized peak shapes. The DSE also naturally delivers full information on the influence of particle size and morphology on diffraction patterns. Since questions of computation time have not been addressed so far, a discussion of this is given in the following section. To round off, a prognosis of necessary future work is given in §8.3, in order to develop points that have arisen in this article.

Table 5
Representative elapsed times (s) for stage 1 measured under three different conditions.

Condition A: with the Compaq Visual Fortran compiler version 6.1.0; condition B: with the Intel Fortran 9.0 compiler for a single processor; condition C: with the Intel Fortran 9.0 compiler for two processors running in parallel. Test crystallites were equiaxial with the lengths specified. Δr = 0.01 Å. Atomic displacement parameters were also applied.

Crystallite length (nm), compiler condition	NaCl	Quartz	PZT	Kaolinite (no H) $\varphi_{dis} = 0$	Kaolinite (with H) $\varphi_{dis} = 0$
40, A	2	7	11	20	35
40, B	5	14	22	43	74
40, C	2	5	7	14	24
80, A	22	58	86	161	283
80, B	43	112	180	348	611
80, C	18	41	60	116	192
120, C	62	138	202	396	652
160, C	149	329	485	938	1547
200, C	293	652	951	1861	3065

8.2. Issues of computation time

8.2.1. Stage 1. The rate-determining step in the algorithm for calculating p.d.f.'s corresponds to the calculation of lengths r of the interatomic vectors as sums of lattice- and cell-pair vectors [equation (2)]. Since the number of times a particular lattice-pair vector will arise in a given crystallite, $N(n_x, n_y, n_z)$, is conveyed by equation (3), the calculation of the length of a given lattice-pair vector, r, only needs to be carried out once, instead of $N(n_x, n_y, n_z)$ times. Thus a factor of acceleration may be calculated, which is given by the ratio of the number of distance calculations in a conventional algorithm to the number of distance calculations in the new algorithm.

In a conventional algorithm, atom pairs are considered one by one. If no interactions are counted twice, the number of distance calculations for a cluster of N_{atom} atoms will be given by $\frac{1}{2}N_{atom}(N_{atom} + 1)$. N_{atom} is given by the product of the number of atoms in the unit cell and the number of unit cells in the crystallite. If the simplifying assumption is made that there are equal numbers of unit cells along all three axes, $L_x = L_y = L_z = L$. Thus $N_{atom} = N_{uc}L^3$, with N_{uc} the number of atoms in the unit cell.

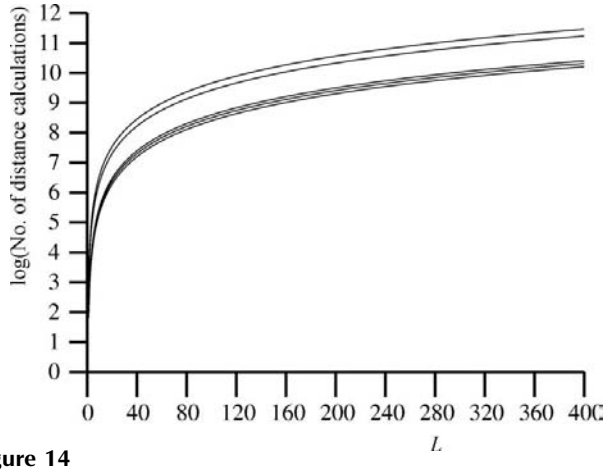

Figure 14
Dependence of number of distance calculations on number of unit cells along all three axes for the following systems (from bottom to top curve): NaCl, quartz, PZT, kaolinite (without H atoms), kaolinite (with H atoms).

From §4.2, the number of different lattice-pair vectors in the new method is equal to $\frac{1}{2}[(2L_x - 1)(2L_y - 1)(2L_z - 1) - 1]$. For the simplified crystallite this product is equal to $4L^3 - 6L^2 + 3L - 1$. The number of distance calculations is obtained by multiplying the result by the number of different cell-pair vectors, which is approximately equal to but always less than N_{uc}^2. To this are added N_{uc}^2 distance calculations for the case $n_x = n_y = n_z = 0$. Thus the number of distance calculations, N_{calc}, is given by $N_{uc}^2(4L^3 - 6L^2 + 3L)$ and the theoretical factor of acceleration by

$$f_{accel} = \frac{L^3 + (1/N_{uc})}{2[4 - (6/L) + (3/L^2)]} \simeq \frac{L^3}{8[1 - (3/2L)]}, \quad (L \gg 1). \tag{10}$$

Thus for a crystallite of dimensions 50 × 50 × 50 unit cells, L = 50 and the factor of acceleration will be approximately 16 108. A calculation using a traditional Debye algorithm with an execution time of 5 min will now take 0.02 s.

In spite of this convincing factor of improvement, the number of distance calculations in the new method, N_{calc}, is strongly dependent on L, as shown in Fig. 14 for the relevant N_{uc} values: NaCl: 8; quartz: 9; PZT: 10; kaolinite (no H): 26: kaolinite (with H): 34.

The conversion of values of N_{calc} into an elapsed execution time depends on the computer, the code and the compiler. The total elapsed time will be approximately equal to $N_{calc}t_{calc}$, where t_{calc} is the time taken for a distance calculation. The elapsed times quoted in Table 5 were measured on a standard PC equipped with an IntelCore2 Duo CPU E6850 processor running at 3.00 GHz.

Compilation conditions A, B and C are compared for the smallest crystallites, from which a trend emerges. In view of superiority of conditions C, under which the code is executed in parallel, only these values are quoted for the three larger crystallites. The dependence of elapsed time on crystallite length d and number of atoms in the unit cell is broadly consistent with Fig. 14. The absolute values of time quoted here indicate how there is scope for further optimization of the calculations, as discussed in §8.3.

Table 6
Representative elapsed times (s) for stage 2 measured under the three different conditions used in Table 5.

$\Delta(2\theta) = 0.02^\circ$.

Crystallite length (nm), compiler condition	NaCl	Quartz	PZT	Kaolinite (no H) $\varphi_{dis} = 0$	Kaolinite (with H) $\varphi_{dis} = 0$
40, A	19	81	338	256	893
40, B	20	82	340	257	900
40, C	10	44	147	107	371
80, A	85	174	742	550	1949
80, B	85	174	743	550	1947
80, C	46	90	314	217	776
120, C	87	138	496	328	1176
160, C	127	184	639	438	1562
200, C	168	230	798	545	1952

8.2.2. Stage 2. An evaluation of the computation times at stage 2 is of less importance, as no innovative techniques were developed here. Furthermore, it is intended to dispense with the calculation of p.d.f.'s as an intermediate stage in future work, thereby making stage 2 redundant. In outline, the computation time is directly proportional to the number of occupied bins in the p.d.f., to the number of partial p.d.f.'s (*i.e.* different atom pair–temperature factor combinations) and to the resolution of the Q values of the diffraction pattern, *i.e.* $1/(\Delta Q)$. The number of occupied bins increases with crystallite size, decreasing bin width Δr and decreasing crystal symmetry. Representative values, which relate to the systems examined here, are quoted in Table 6.

Unlike in stage 1, compilation conditions A and B lead to similar results, although the superiority of conditions C is again apparent. Within a particular system, the elapsed times scale approximately linearly with crystallite length d.

8.3. Future work

Further progress in the use of the DSE to model powder diffraction patterns will require the development of an analytical framework to cross-relate the DSE language of lattice-pair and cell-pair vectors with the Bragg–Rietveld language of lattice planes and atomic coordinates. At present the DSE method is unwieldy because of the calculation of p.d.f.'s as an intermediate stage. It is desirable to be able to relate changes in pair vectors directly to changes in diffraction pattern. Owing to the linearity of the $(\sin Qr)/Qr$ transformation, this should be possible, as is also suggested by the observation of partial diffraction patterns in §4.5. The adoption of a direct calculation from pair vectors to diffraction pattern would also allow a full treatment of anisotropic displacement parameters. At present the necessary directional information for this is destroyed by the intermediate p.d.f. encoding.

No explicit use has been made of crystal symmetry in the present work. However the separation of cell-pair vectors from lattice-pair vectors offers the potential for further reductions in computation time here, both because of the centrosymmetry of the set of cell-pair vectors and because of equivalent sets of lattice-pair vectors. In addition, the field of lattice-pair vectors has been mined inefficiently in the present work, with benefits to be gained by treating collinear vectors together. The inclusion of these factors will allow a further reduction in the number of explicit distance calculations and therefore computation time.

Once these issues have been addressed, the potential arises of a direct dialogue between the DSE approach and the Rietveld structural refinement method, where the obvious advantage of having fewer adjustable parameters in the DSE approach presents itself.

On the application side, refinements in the modelling of disordered structures are called for. Limitations in the random-number-generator approach have been identified, pointing towards the need for a more analytical treatment. The extension to more complex types of structural disorder, for example turbostratic disorder in 2:1 clay minerals, would be a fruitful direction for further work. In addition, the derivation of modified equations for $N(n_x, n_y, n_z)$, to apply to crystal habits other than parallelepipedal, would be a welcome development.

The continuous progression in calculated diffraction patterns from nano- to microscales suggests that the DSE method could be developed to gain a handle on particle-size distributions at the very fine end. This would also be relevant for a quantitative treatment of the mineralogy of plastic clays, since the main issues of crystalline disorder and fine particle sizes both affect the observed diffraction patterns in different ways.

The Application Support Team of PANalytical BV in Almelo and Professor Dr Gerold Brachtel are thanked for helpful discussions.

References

Artioli, G., Bellotto, M., Gualtieri, A. & Pavese, A. (1995). *Clays Clay Miner.* **43**, 438–445.
Bish, D. L. (1993). *Clays Clay Miner.* **41**, 738–744.
Debye, P. (1915). *Ann. Phys. (Leipzig)*, **46**, 809–823.
Frantti, J., Lappalainen, J., Eriksson, S., Lantto, V., Nishio, S., Kakihana, M., Ivanov, S. & Rundlof, H. (2000). *Jpn. J. Appl. Phys.* **39**, 5697–5703.
Gnutzmann, V. & Vogel, W. (1990). *J. Phys. Chem.* **94**, 4991–4997.
Grover, R. F. & McKenzie, D. R. (2001). *Acta Cryst.* A**57**, 739–740.
Hall, B. D. (2000). *J. Appl. Phys.* **87**, 1666–1675.
International Tables for X-ray Crystallography (1974). Vol. IV, edited by J. A. Ibers & W. C. Hamilton. Birmingham: Kynoch Press.
Kihara, K. (1990). *Eur. J. Mineral.* **2**, 63–77.
Makinson, J. D., Lee, J. S., Magner, S. H., De Angelis, R. J., Weins, W. N. & Hieronymus, A. S. (2000). *Adv. X-ray Anal.* **42**, 407–411.
Nelmes, R. J. (1969). *Acta Cryst.* A**25**, 523–526.
Pinna, N. (2005). *Prog. Colloid Polym. Sci.* **130**, 29–32.
Pinna, N., Wild, U., Urban, J. & Schlögl, R. (2003). *Adv. Mater.* **15**, 329–331.
Plançon, A. & Tchoubar, C. (1975). *J. Appl. Cryst.* **8**, 582–588.
Rietveld, H. M. (1969). *J. Appl. Cryst.* **2**, 65–71.
Tettenhorst, R. T. & Corbató, C. E. (1988). *Clays Clay Miner.* **36**, 181–183.

Treacy, M. M., Newsam, J. M. & Deem, M. W. (1991). *Proc. R. Soc. London*, **433**, 499–520.
Trueblood, K. N., Bürgi, H.-B., Burzlaff, H., Dunitz, J. D., Gramaccioli, C. M., Schulz, H. H., Shmueli, U. & Abrahams, S. C. (1996). *Acta Cryst.* A**52**, 770–781.
Vogel, W. (1998). *Cryst. Res. Technol.* **33**, 1141–1154.
Walker, D., Verma, P. K., Cranswick, L. M. D., Jones, R. L., Clark, S. M. & Buhre, S. (2004). *Am. Mineral.* **89**, 204–210.
Warren, B. E. (1934). *Phys. Rev.* **45**, 657–661.
Warren, B. E. (1969). *X-Ray Diffraction*. Massachusetts: Addison-Wesley.
Wilson, A. J. C. (1942). *Proc. R. Soc. A*, **180**, 277–285.